L- and *M*-shell-electron shake processes following 1*s* photoionization in argon and krypton

J.-Cl. Dousse and J. Hoszowska
Physics Department, University of Fribourg, CH-1700 Fribourg, Switzerland
(Received 28 February 1997)

The photoinduced $K\alpha$ and $K\beta$ x-ray spectra of argon and krypton were measured by means of high-resolution crystal diffractometry. Ar $K\alpha_{1,2}L^{(1)}$ and $K\beta_{1,3}M^{(1,2)}$ and Kr $K\alpha_1L^{(1)}$ and $K\beta_2M^{(1,2)}$ satellites were observed and resolved from the corresponding diagram lines. From the satellite to parent diagram line yield ratios, the probabilities for producing via shake processes $K^{(1)}L^{(1)}$ and $K^{(1)}M^{(1)}$ double-hole states were deduced. The results are compared to the few other existing experimental data and to theoretical sudden approximation predictions. The latter are found to underestimate somewhat the experimental values. [S1050-2947(97)01612-0]

PACS number(s): 32.30.Rj, 32.80.Fb, 34.50.Fa

I. INTRODUCTION

Atomic inner-shell photoionization is a rather weak process, in a perturbation sense, in which a single photon can be assumed to interact with a single bound electron. Direct multiple ionization caused by photoionization can thus be considered as negligibly small. Excited atomic states with more than one inner-shell vacancy are, however, frequently observed as a result of photoionization. This multiple excitation may originate from the nonradiative decay of the photoinduced initial single-hole state. Auger and Coster-Kronig transitions are examples of such autoionizing processes. As a consequence in light elements, where nonradiative decay processes dominate, photoionization leads, in most cases, to multiply ionized atoms.

The observation in x-ray [1–3], Auger [4], and photoelectron spectra [5] of satellites emitted when the primary excited states decay proves that processes other than radiationless transitions do contribute to the multiple excitation. This statement is confirmed by the excitation features observed in photoabsorption spectra [6]. In fact, due to the sudden change of the atomic potential following the removal of a core electron by the photon impact, other electrons can be ejected into the continuum (shakeoff) or promoted to higher unoccupied bound states (shakeup) [1,3,7].

Shake probabilities do not depend, in first order, on the mechanism leading to the creation of the core vacancy. As a consequence, shakeoff and shakeup may also result from internal conversion of nuclear γ rays [8] or from collisions with charged particles [9]. Since the potential affecting an electron is made up of the nuclear charge minus the shielding of the other electrons, shake excitations can furthermore be initiated by nuclear decay, such as α decay, β decay, and electron capture. In this case the shaken electron is promoted into the continuum or unfilled higher shells by the abrupt change of the nuclear charge [10,11].

The observation of shake effects resulting from internal conversion of γ rays is usually based on measurements of *K* conversion-electron spectra. Radioactive sources with long enough lifetimes are needed in such experiments. This limits the number of elements which can be studied by means of this method. In experiments dealing with shake processes induced by nuclear decay, radioactive isotopes of the elements to be studied are also needed. In addition, as a result of nuclear decay, many excited states of the final nucleus are populated. It is then a hard task to determine which shake events are due to the change of the nuclear charge and which ones result via internal conversion from γ transitions in the final nucleus. In collision experiments shake effects are difficult to distinguish from multiple ionization induced by the charged particle impact. The direct Coulomb ionization cross section is proportional to the squared charge of the projectile. It decreases with the projectile velocity as long as the latter is higher than the orbital velocity of the ionized electron. Therefore only high-energy collisions involving light charged particles like electrons or protons can be considered within this method to get reliable shake probabilities.

Such problems or experimental difficulties are not encountered in the case of photoionization. At photon energies higher than about 1.3 times the energy threshold for double ionization, the shake probability is nearly energy independent [7,12] and the probability for the outgoing electron to collide with another bound electron and to eject it (two-step-one process) vanishes [12,13]. As a consequence, satellite yields observed in photoelectron spectra can be assumed to result quasiexclusively from shake processes. The same holds for *K* x-ray spectra, whereas for *L* and *M* x-ray spectra, *LLX* and *MMY* Coster-Kronig transitions taking place prior to the x-ray emission can contribute significantly to the observed satellite yields [14]. For the above-mentioned reasons, most of the available experimental data concerning shake effects have been obtained in photoionization experiments. In addition, recent developments in experimental techniques have led to a renewed interest for photoinduced processes. In this respect, synchrotron radiation facilities which deliver very intense and energy-tunable x-ray beams have certainly played a major role.

The energy left in the atom for the shake excitation of the second electron results in a reduction of the kinetic energy of the first ejected electron. In photoelectron spectra complex satellite structures that include discrete peaks (shakeup) and continuous features (shakeoff) are therefore observed on the low kinetic energy side of the primary peaks [5,15,16]. In x-ray spectroscopy satellite structures are also observed but, in this case, on the high-energy side of the main lines. Due to the second core vacancy created by the shake process, the

screening of the nuclear charge is reduced, which results in an increase of the binding energies of the atomic levels. As this binding energy enhancement decreases with the principal quantum number of the levels, x-ray satellites are emitted at higher energies than the parent diagram lines.

The energy shifts of satellite x rays increase with the principal quantum number of the transition electron and decrease with the principal quantum number of the spectator vacancy. For midheavy atoms $K\alpha L^{(1)}$ and $K\beta L^{(1)}$ satellites (i.e., $K\alpha$ and $K\beta$ x rays emitted with one additional hole in the L shell) are shifted with respect to the parent diagram transitions by 40–60 eV [17] and 100–150 eV [18], respectively. Energy shifts of K x rays originating from the radiative decay of $K^{(1)}M^{(1)}$ states are approximately ten times smaller, i.e., nearly equal to the natural linewidths of the corresponding transitions [17,19]. For this reason, M satellites cannot be resolved in general from the close-lying parent diagram lines. Only a broadening of the latter and/or a slight asymmetry appearing on their high-energy flanks reflects then the additional M-shell ionization. The $K\beta_2$ transition constitutes a very interesting exception to this general rule. Due to the fact that in this case the transition electron originates from the outer subshells $N_{2,3}$, the energy shifts are larger than in other K x-ray transitions. As a consequence, $K\beta_2 M^{(1,2)}$ satellites appear in the $K\beta$ x-ray spectra of medium-mass atoms as single, well-resolved lines [18,19]. For lighter elements like argon, which are characterized by narrower linewidths, M satellites are better separated from the main lines and usually they can be resolved from the parent $K\beta_{1,3}$ transitions.

Taking advantage of these properties and assuming, as discussed above, that satellite features observed in photoinduced K x-ray spectra arise entirely from shake effects, we have determined the probabilities for L- and M-electron shake processes following $1s$ photoionization in krypton and argon. The krypton and argon K x-ray spectra were measured by means of high-resolution crystal spectroscopy. The L- and M-shell shakeoff plus shakeup probabilities were deduced from the observed yield ratios $I[K\alpha_1 L^{(1)}]/I[K\alpha_1 L^{(0)}]$ and $I[K\beta_2 M^{(1,2)}]/I[K\beta_2 M^{(0)}]$ for Kr and $I[K\alpha_{1,2} L^{(1)}]/I[K\alpha_{1,2} L^{(0)}]$ and $I[K\beta_{1,3} M^{(1,2)}]/I[K\beta_{1,3} M^{(0)}]$ for Ar.

II. EXPERIMENT

The measurements of the photoinduced K x-ray spectra were performed at the University of Fribourg by means of two different high-resolution bent crystal spectrometers. The krypton x-ray emission spectra were observed with a DuMond transmission-type crystal spectrometer. As this instrument cannot be used for photon energies below about 10 keV, the argon spectra were measured with a von Hamos reflection-type crystal spectrometer. For both elements, the fluorescence x-ray spectra were produced by irradiating the gaseous targets with the bremsstrahlung of an x-ray tube. The relative intensity I_{tube} of the x-ray tube radiation contributing to the $K^{(1)}$, $K^{(1)}L^{(1)}$, or $K^{(1)}M^{(1,2)}$ excitation of the target and the corresponding average energy $\overline{E}_{\text{tube}}$ were computed with a dedicated program, using the measured spectral and angular distributions of the bremsstrahlung emitted by the x-ray tube and the photoionization cross sections quoted by Storm and Israel [20]. The intensity attenuation of the ionizing radiation in the wall of the gaseous target cell and in the gas were taken into account in these calculations, whose results are given in Table I.

TABLE I. Characteristics of the photon beams used for the irradiation of the targets.

Target	X-ray tube	Excited state	I_{tube}	$\overline{E}_{\text{tube}}$ (keV)	ϵ_{KS}[a]	ξ_{KS}[a]
Kr 3 bars	Au 80 kV	$K^{(1)}$	1000	25.1		
		$K^{(1)}L^{(1)}$	891	26.3	5.60	0.65
Kr 1 bar	Au 80 kV	$K^{(1)}$	1000	23.0		
		$K^{(1)}M^{(1)}$	984	23.1	52.0	0.23
Ar 2 bars	Cr 50 kV	$K^{(1)}$	1000	8.66[b]		
		$K^{(1)}L^{(1)}$	968	8.81	18.3	0.31
Ar 2 bars	Cr 50 kV	$K^{(1)}$	1000	8.53[b]		
		$K^{(1)}M^{(1)}$	998	8.54	286	0.08

[a]See Eqs. (5) and (6) (the mean radii $\langle r_L \rangle$ and $\langle r_M \rangle$ were taken from Ref. [63]).

[b]The difference between the two energies has a geometrical origin (the target slice affecting the crystal through the slit was indeed located closer to the x-ray tube in the $K\beta$ measurement than in the $K\alpha$ one).

A. Krypton measurements

The main characteristics of the DuMond curved crystal spectrometer of Fribourg were already presented in several previous articles (see, e.g., [14,21,22]). Thus, in the following, only the features specific to the experimental setup used for the krypton measurements will be discussed.

The spectrometer was operated in a so-called modified DuMond slit geometry. As shown in Fig. 1(a), in this geometry the target is viewed by the bent crystal through a narrow slit located on the focal circle. The 0.1-mm-wide slit was made of two vertical juxtaposed Pb plates, 25 mm high and 5 mm thick. The target consisted of a cylindrical cell filled up with 99.99% pure krypton. The cell was 3 cm in diameter and 3 cm high with an 11-mg/cm^2-thick kapton wall. The distance between the slit and the axis of the target was 2.75 cm. The K x-ray emission was induced by means of an x-ray tube with a Au anode and a thin Be window. The distance between the tube anode and the target center was 4.5 cm and the axis of the conical beam emitted by the x-ray tube was perpendicular to the target-crystal direction (see Fig. 2). The emission angle of the ionizing radiation covered the complete volume of the gaseous target but, due to the slit, only a vertical slice, 25 mm high$\times$30 mm long$\times$0.1 mm thick, contributed to the production of the observed krypton K x rays. The tube was supplied with a 100-kV/3-kW high voltage generator equipped with a dedicated system for the stabilization of the current and high voltage.

For the diffraction of the x rays, the (110) reflecting planes of a 10$\times$10-cm^2 quartz crystal plate, 0.5 mm thick, were used. The choice of such a thin crystal was dictated by the strong intensity attenuation suffered by low-energy photons in the case of Laue diffraction. For instance, with a 1-mm-thick crystal the observed intensity of the krypton $K\alpha_1$ line would have been about four times smaller. The

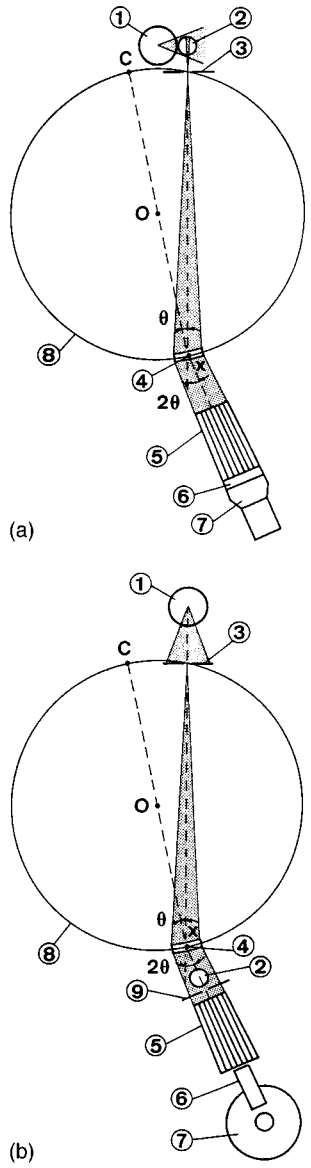

FIG. 1. Schematic view of the transmission-type crystal spectrometer (not to scale). (a) The modified DuMond slit geometry used in this experiment. (b) The experimental setup used for the measurement of the K absorption edge. [1: x-ray tube, 2: target cell, 3 and 9: lead slit, 4: bent crystal, 5: Soller-slit collimator, 6: Phoswich scintillator in (a) or LeGe detector in (b), 7: photomultiplier in (a) or LN_2 Dewar in (b), 8: Rowland circle. θ represents the Bragg angle, X the crystal axis, C the center of curvature of the crystal, and O the center of the focal circle.]

quartz lamina was bent cylindrically to a radius $R = 311.6$ cm by means of a bending device similar to the one described in [23]. The effective reflecting area of the crystal was 12 cm^2. The instrumental response of the spectrometer which depends mainly on the slit width and precision of the crystal curvature was found to be well reproduced by a Gaussian function with a full width at half maximum (FWHM) of 10.7 arcsec. In the DuMond geometry the angular instrumental response does not vary with the Bragg angle θ according that the crystal-to-slit distance d is adjusted for each x-ray line to $d = R \cos\theta$. For the $K\alpha_1$ and $K\beta_2$ transitions of krypton, that were measured at focal distances of

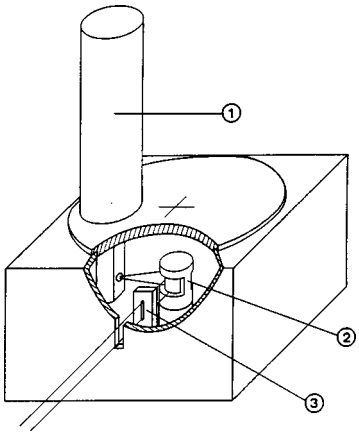

FIG. 2. Target chamber of the DuMond curved crystal spectrometer (1: x-ray tube, 2: target cell, 3: lead slit).

305.3 and 306.7 cm, the above-mentioned resolution of 10.7 arcsec resulted in instrumental energy broadenings of 3.2 and 4.1 eV, respectively. The Bragg angles were measured by means of an optical laser interferometer [24] with a precision of a few marcsec.

For the detection of the x rays a 5-in.-diam$\times$0.25-in. NaI(Tl) $\times$2-in. CsI(Tl) Phoswich (The Harshaw Chemical Co., Crystal and Electronic Products Dept., OH 94139) scintillation detector [14] was employed. This type of detector presents the advantage to strongly diminish the Compton noise arising from high-energy photons. A further diminution of the background was achieved by enclosing the Phoswich detector in a heavy Pb-Cu-Al shielding and by sorting on line the events of interest as a function of their energy. In order to reduce the absorption of x rays in air, evacuated tubes were mounted between the target chamber and the crystal and between the crystal and the 66-cm-long Soller-slit collimator. The latter and the target chamber were also pumped down to about 1 mbar.

The $K\alpha_{1,2}$ x-ray spectrum of krypton is shown for illustration in Fig. 3(a). For this measurement the x-ray tube was operated at 80 kV$\times$30 mA and the gaseous target density was 9.50 mg/cm^3 (pressure of $\sim$3 bars). The spectrum was measured in approximately 14 h (128 points with an acquisition time of 400 sec per point). As the probability for creating the $K^{(1)}L^{(1)}$ states through shake processes is very small in the case of krypton, the angular range of the $K\alpha_1 L^{(1)}$ satellite region was remeasured in eight successive step-by-step scans. Each scan consisted of 50 points and the acquisition time per point was 1400 sec. In order to survey the reliability of the measurements and the stability of the experimental setup, a shorter control measurement of the $K\alpha_1$ diagram line was performed between each scan. The intensity variations observed in these control measurements were found to be consistent with 1σ fluctuations. Regarding the position of the $K\alpha_1$ centroid, no systematic shift as a function of time was observed, the average fluctuations being of the order of 40 marcsec (i.e., about 12 meV). Thus no *a posteriori* intensity normalization of the different scans, nor an energy adjustment, was performed and the $K\alpha_1 L^{(1)}$ satellite x-ray spectrum depicted in Fig. 3(b) was simply built up by summing off line the eight scans. For the energy calibration of the spectrum, the energy of the $K\alpha_1$ transition

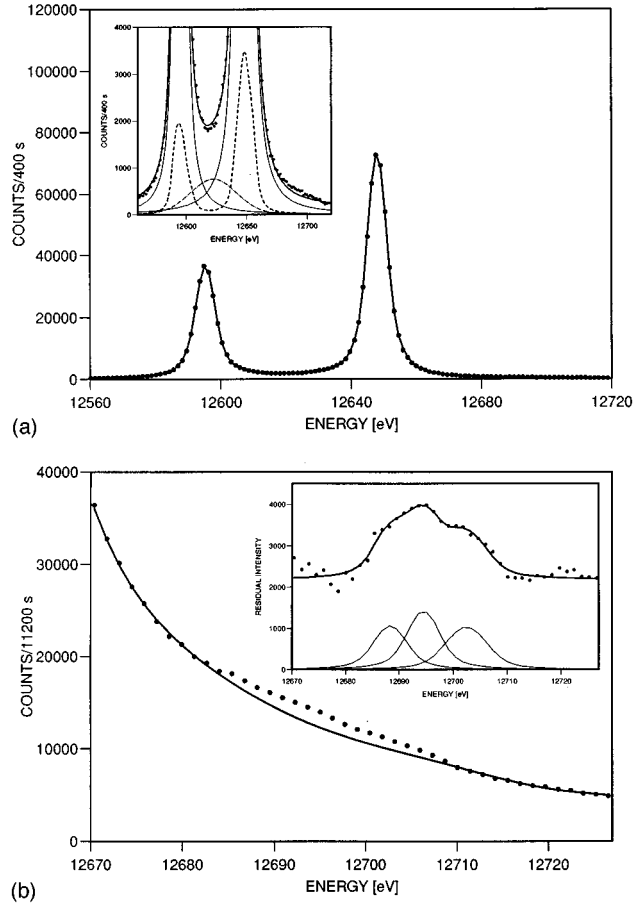

FIG. 3. (a) $K\alpha_{1,2}$ x-ray spectrum of Kr. Details of the fit are shown in the inset (the thick solid line represents the total fit, the thin solid lines the fit of the diagram transitions, the dashed lines the fit of the unresolved M satellites, and the dash-dotted line the fit of the KLN RAE structure). (b) $K\alpha_1 L^{(1)}$ x-ray satellite spectrum superimposed on the high-energy flank of the $K\alpha_1$ diagram transition. The fit of the residual intensity obtained after the subtraction of the $K\alpha_1$ tail (satellite structure) is shown in the inset.

quoted by Bearden and Burr [25] was used, while the origin of the angular scale was determined by measuring the $K\alpha_1$ line at positive and negative Bragg angles. It has to be noted here that, as a result of newer evaluations of certain conversion factors or calibration energies, the Bearden and Burr values were found to be too small by about 13 ppm [26]. In the present experiment, however, only the energy shifts of the satellites with respect to the parent diagram lines are of interest. As these shifts are hardly affected by the differences in the conversion factors, no attempt was made to adjust the Kr $K\alpha_1$ energy quoted by Bearden and Burr.

For krypton the K absorption edge (14.324 keV) lies exactly between the $K\beta_2$ diagram line (14.315 keV) and the $K\beta_2 M^{(1)}$ satellite ($\sim$14.333 keV). The latter is thus much more affected by the self-absorption of the x rays in the target than the parent diagram line. In order to reduce the self-absorption, the $K\beta_2$ measurements were performed with a lower gas density of 3.18 mg/cm^3 (pressure of $\sim$1 bar). The x-ray tube was operated at 80 kV$\times$35 mA. The angular region corresponding to the $K\beta_2$ plus $K\beta_2 M^{(1,2)}$ domain was measured in ten successive step-by-step scans. Each scan consisted of 71 points with an acquisition time of 1000 sec

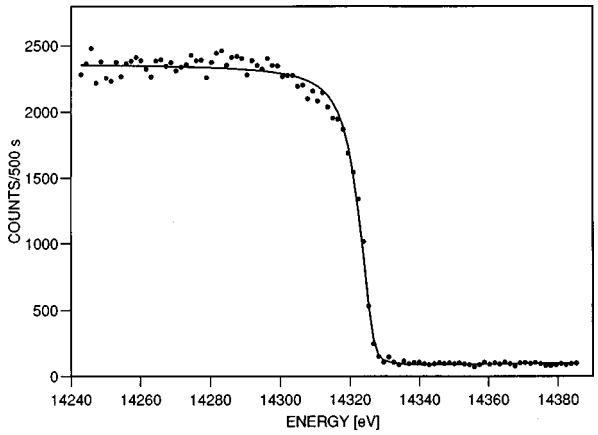

FIG. 4. Krypton K absorption edge (the solid line represents the fit to the data).

per point. During this ten-day long measurement, the intensity fluctuations of the $K\beta_2$ line were smaller than 1% but some time-dependent shift towards higher energies of the line centroid was observed. However, the energy difference of the $K\beta_2$ centroid between the first and the last scan being only $\sim$0.3 eV, no correction was performed and the ten scans were simply added together.

The $K\beta_2$ spectrum was corrected for the self-absorption in the target. To determine the variation of the krypton absorption coefficient as a function of the photon energy in the K-edge region, the K absorption edge of krypton was measured by means of the experimental setup represented in Fig. 1(b). In this measurement the spectrometer was used as a monochromator, the anode of the x-ray tube being viewed directly by the crystal through the slit. A tube with a Cr anode was employed because some characteristic L x rays of Au lie close in energy to the K absorption edge of krypton. The krypton target cell itself (pressure increased to $\sim$3 bars) was used as an absorber and mounted in front of the Soller-slit collimator. A 10-mm-wide Pb slit was further installed between the cell and the collimator, defining an almost constant absorber thickness of 29.4 mg/cm^2. In order to improve the separation of the photons of interest, diffracted by the crystal in first order of reflection, from those diffracted in second order, the Phoswich scintillator was replaced in this measurement by a 5-cm-diam$\times$1-cm-thick LeGe semiconductor detector. As the K-edge and the $K\beta_2$ spectrum were observed at the same focal distance, a single energy calibration was needed for both measurements. The latter was performed by measuring the $K\beta_{1,3}$ line of krypton on both sides of reflection and by using the energy of the $K\beta_1$ transition from [25]. The observed K absorption edge of krypton is shown in Fig. 4. It was fitted with the following function [27]:

$$I(E)=c_1\frac{\eta_0}{(\eta_0^2+1)^{1/2}}+c_2\frac{1}{(\eta_1^2+1)^{1/2}}+c_3, \qquad (1)$$

where the c_i are scaling parameters and the η_i are defined as follows:

$$\eta_{0,1}=\frac{E-E_{0,1}}{w_{0,1}}. \qquad (2)$$

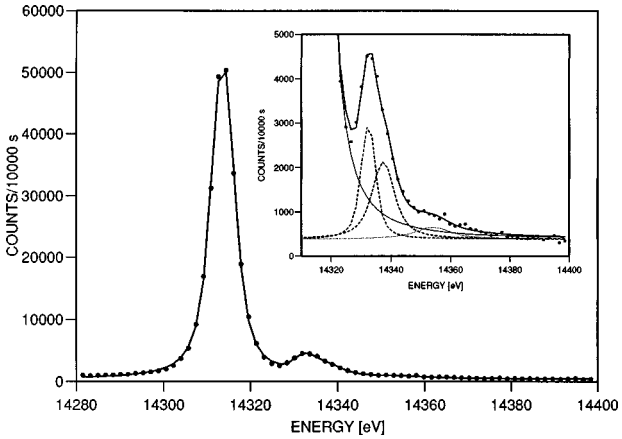

FIG. 5. $K\beta_2$ x-ray spectrum of Kr with resolved M satellites. Details about the fit of the satellites are shown in the inset (dashed lines: first-order satellites; dotted line: second-order satellites; thin solid line: tail of the diagram transition; thick solid line: total fit).

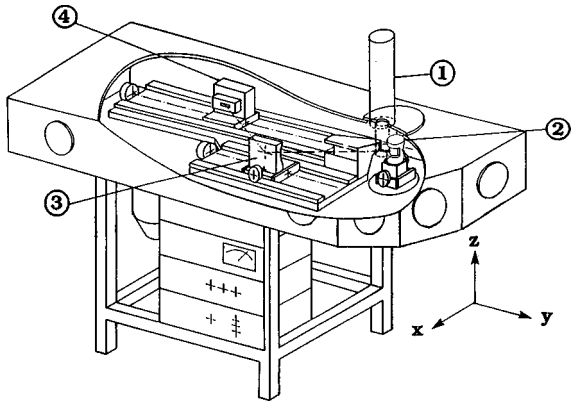

FIG. 6. von Hamos reflecting-type crystal spectrometer. (1: x-ray tube, 2: target cell, 3: bent crystal, 4: CCD detector system. The direction of dispersion is parallel to the y axis.)

The fitted energies E_0 and E_1 were found to be 14 324 and 14 327 eV, respectively, whereas values of 5.8 and 3.0 eV were obtained for the widths w_0 and w_1.

To determine which part of the background had to be subtracted from the $K\beta_2$ spectrum before correcting the latter for the self-absorption in the target, a careful investigation of the background was done. The latter was found to originate from natural radioactivity (47.8%) and from the coherent (47.9%) and incoherent (3.3%) scattering by the target of the radiation emitted by the x-ray tube at $\sim$14.3 keV (coherent) and $\sim$14.7 keV (incoherent). This study showed also that some broad structures were present in the coherent part of the background. These structures were identified as weak Au L transitions. Furthermore, in the detector energy spectrum the Compton front of the photopeaks corresponding to higher-order diffractions was found to contribute also to the measured background, but only $\sim$1%. The $K\beta_2$ spectrum was thus corrected in the following way: the natural background was first subtracted from the raw spectrum. The latter was then corrected for the self-absorption in the target. Finally, the coherent background was subtracted from the corrected spectrum in order to suppress the above-mentioned Au L x-ray contamination. The resulting $K\beta_2$ spectrum is depicted in Fig. 5.

B. Argon measurements

As the observation of photons below 10 keV requires a reflecting-type x-ray spectrometer, the argon measurements were performed with our new von Hamos curved crystal facility [28]. The principal elements of this instrument are an x-ray source defined by a rectangular slit, a cylindrically bent crystal, and a position sensitive detector (Fig. 6). In the von Hamos geometry the crystal is bent around an axis which is parallel to the direction of dispersion (y direction) and provides focusing in the nondispersive z direction. For a fixed position of the components, the impact coordinate on the detector of a reflected x ray corresponds geometrically to a particular Bragg angle and hence to a particular photon energy. Such geometry permits at one position of the spectrometer components data collection over an energy bandwidth which is limited by the detector length. In order to study a greater energy interval the central Bragg angle is adjusted by translation of the crystal and correspondingly of the detector along their axes. The slit-to-crystal and crystal-to-detector distances are varied but kept equal. The target, crystal, and detector are all contained in a $180\times62\times24.5$-cm^3 stainless steel vacuum chamber, which can be pumped down to about 10^{-7} mbar by a turbomolecular pump.

The same target cell as the one used in the krypton measurements was employed. The cell was filled up with 99.99% pure argon. The gas density was 3.08 mg/cm^3 (pressure of $\sim$2 bars). The vertical rectangular slit consisted of two juxtaposed Ta pieces 0.3 mm thick and 10 mm high. The slit width was 37 μm for the $K\alpha_{1,2}$ measurements and 25 μm for the $K\beta_{1,3}$ ones. A very thin sheet of black paper was installed in front of the slit to protect the detector from the visible light emitted by the irradiated gaseous target. The argon fluorescence spectra were produced by means of a Cr x-ray tube operated at 50 kV$\times$35 mA. The target axis was located at a distance of 2 cm from the tube anode and 1.6 cm from the slit. The angle between the mean direction of the ionizing radiation and the slit-to-crystal direction was approximately 210°.

For the diffraction of the x rays the spectrometer was equipped with a 10-cm-high (z extension)$\times$5-cm-wide$\times$0.5-mm-thick quartz (110) crystal. The Bragg angle domain covered by the von Hamos spectrometer extends from 24.4° to 61.1°. For the quartz (110) crystal (lattice spacing constant $2d=8.5096$ Å), the corresponding energy interval is thus comprised between 1.645 and 3.563 keV, i.e., well matched to the K x-ray spectra of argon. The crystal lamina, glued to an Al block machined to a precise concave cylindrical surface, had a nominal bending radius of 25.4 cm. The measurements, however, were performed at a focusing distance of 24.5 cm, for which a better resolution was obtained.

The x rays were recorded with a CCD (charged coupled device) position sensitive detector 27.65 mm long and 6.9 mm high, having a depletion depth of 50 μm and consisting of 1024 columns and 256 rows with a pixel size of 27 μm $\times$27 μm. The diffracted x rays hitting the CCD build a two-dimensional pattern on the detector plane. The horizontal axis of the detector corresponds to the energy axis of the x-ray spectrum, while the vertical extension of the detector

in the z direction serves mainly to collect more intensity. The CCD detector was thermoelectrically cooled down to $-60\,^{\circ}$C. It was operated by a ST-138 controller (Princeton Instruments, Inc.) equipped with a DMA/TAXI high-speed serial interface which can sustain data transfer to a PC at 1 Mbyte/sec.

The instrumental energy resolution of the von Hamos spectrometer is determined by the finite size of the slit aperture, Darwin diffraction width of the crystal, spatial resolution of the detector, and focusing aberrations. For the setup used in the argon experiment, the profile of the instrumental response could be approximated quite well by a 0.8-eV FWHM Lorentzian.

For data acquisition and analysis of images a dedicated software package written specifically to operate the ST-138 controller was used. The time of a single acquisition was chosen depending on the count rate, so that multiple hits on one pixel were minimized. Thanks to the good energy resolution of the CCD detector, higher-order reflections and background events could be rejected by setting appropriate energy windows. The data were taken in a repetitive accumulation mode. Each image corresponding to a separate acquisition was filtered. Then the different images were summed and the resulting two-dimensional spectrum was projected on the y axis to give the one-dimensional position spectrum. The 27-μm pixel resolution being not really needed in this experiment, a software binning of four columns was performed in order to obtain higher count rates in the position spectrum. Finally the position spectra were calibrated in energy by means of the formulas (3) and (4) given in [28], using the $K\alpha_1$ energy quoted by Deslattes and Kessler [29] as reference.

For the $K\alpha_{1,2}$ x-ray spectrum 2100 images were collected with an acquisition time of 10 sec per image. For the $K\beta_{1,3}$ spectrum 950 images were taken with an exposure time of 60 sec each. The time needed to open (at the beginning of each new acquisition) and to close (before the readout of the data) the CCD shutter is 0.2 sec so that the total effective times used to measure the $K\alpha_{1,2}$ and $K\beta_{1,3}$ spectra of argon were $\sim$20 100 and $\sim$56 600 sec, respectively. Both spectra were corrected for the self-absorption in the gas and for the intensity attenuation by the kapton wall. The solid angle under which a single CCD column is seen by a source point depends on the Bragg angle (i.e., the energy). This effect was taken into account in the correction procedure. On the contrary, the influence of the K absorption edge of argon was neglected, only the high-energy tail of the second-order $K\beta_{1,3}M^{(2)}$ satellite being affected by it. Possible fluctuations of the detector efficiency along the direction of dispersion were checked. No statistically significant variation was observed. Furthermore, the crystal reflectivity was assumed to be constant over the whole surface contributing to the diffraction. The corrected $K\alpha_{1,2}$ and $K\beta_{1,3}$ x-ray spectra of argon are presented in Figs. 7 and 8, respectively.

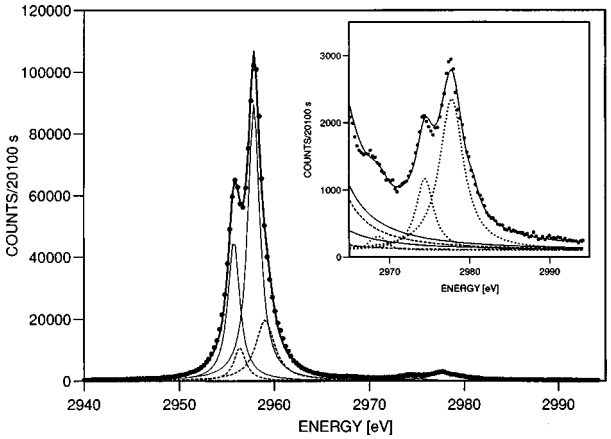

FIG. 7. Ar $K\alpha_{1,2}$ x-ray spectrum. The L-satellite structure is shown enlarged in the inset. The thin solid lines correspond to the fit of the diagram transitions, the dashed ones to the fit of the unresolved M satellites, the dotted ones to the fit of the L-satellite components whereas the thick solid line represents the fitted spectrum.

III. DATA ANALYSIS

A. General considerations

The observed K x-ray spectra were analyzed by means of the least-squares-fitting computer program MINUIT [30] (CERN library). For krypton Voigt profiles were employed to fit the diagram and satellite lines. The convolution of the Gaussian instrumental broadening of the DuMond spectrometer with the Lorentzian function representing the natural line shape of an x-ray transition results indeed in a Voigt profile. For argon, Lorentzian functions were used since the von Hamos instrumental response could be well reproduced by a Lorentzian profile. However, because the observed satellite lines consisted of many overlapping components, most of them could not be fitted with a single Voigt or Lorentz profile. The same held for those diagram transitions for which an asymmetric shape resulting from unresolved satellites was observed. For this reason, we tried first to perform the analysis with the method described in Ref. [31]. In this method which was developed to analyze spectra of multiply ionized atoms, a particular x-ray line is assumed to be a linear combination of all components contributing to the transition. The theoretical energies and transition probabilities of the individual components are determined by means of extensive MCDF (multiconfiguration Dirac-Fock) calculations. The final result of the MCDF calculations is a ''stick'' spectrum consisting of many lines. To compare with experi-

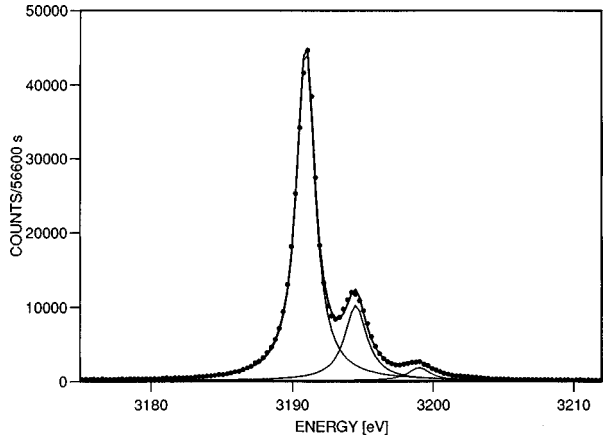

FIG. 8. Fitted Ar $K\beta_{1,3}$ x-ray spectrum with resolved first- and second-order M satellites.

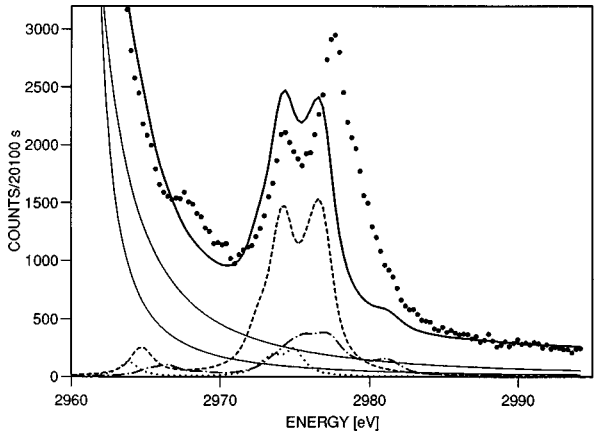

FIG. 9. Tentative fit of the Ar $K\alpha_{1,2}L^{(1)}$ satellites with the MCDF method. The solid line represents the total fit whereas the dashed, the dash-dotted, and the dotted curves represent the fitted satellite shapes corresponding to $[1s^{-1}3d^{-1}]$, $[1s^{-1}3p^{-1}]$, and $[1s^{-1}3s^{-1}]$ initial hole configurations, respectively.

ment the lines are given a Voigtian (krypton) or Lorentzian (argon) shape. The transition line shape is then constructed by computing the weighted sum of the Voigt or Lorentz functions corresponding to the different lines, the weighting factors being given by the transition probabilities of the latter. For both elements the MCDF calculations [32] were performed with the MSAL (modified special average level) version [33] of the GRASP code [34]. The analysis showed, however, that the experimental spectra were not reproduced with a sufficient precision by the theoretical MCDF predictions. This is illustrated in Fig. 9, which represents a tentative MCDF fit of the $K\alpha_{1,2}$ L-satellite region of Ar. The transitions $K^{(1)}L_1^{(1)}\rightarrow L_1^{(1)}L_{2,3}^{(1)}$ (six components), $K^{(1)}L_{2,3}^{(1)}\rightarrow L_{2,3}^{(2)}$ (14 components), and $K^{(1)}L^{(1)}M^{(1)}\rightarrow L^{(2)}M^{(1)}$ (419 components) were considered. A Lorentzian shape with a FWHM of 1.5 eV was given to each component. The absolute energies and transition probabilities of all components were determined by MCDF calculations resulting for the three transitions into complex shapes. As can be seen, the general trends of the measured spectrum are reproduced by the MCDF calculations but systematic deviations in the energies and intensities of the satellite components result in a poor agreement of the theoretical shape with the experimental data. A similar observation was made previously for the $K\beta$ spectrum of argon [35,36]. Thus, for all spectra, a standard fitting procedure was finally chosen, in which one or if necessary several Voigt or Lorentz profiles were employed to reproduce the broadened and/or asymmetric shape of the observed transitions. More details about the fit of the different spectra are given below.

B. Krypton $K\alpha$ spectrum

At first the $K\alpha_{1,2}$ and $K\alpha_{1,2}M^{(1)}$ transitions were fitted with four Lorentz profiles, two for the diagram lines and two for the unresolved M satellites. The Lorentzian width was kept constant at 4.23 eV [37] for the four lines. However, the differences in the natural linewidths and broadenings induced by the N-shell ionization were accounted for by using different Gaussian widths for the $K\alpha_1$, $K\alpha_2$, $K\alpha_1M^{(1)}$, and $K\alpha_2M^{(1)}$ transitions, and by letting free these four parameters in the fitting procedure. An additional constraint was set on the $I[K\alpha_{1,2}M^{(1)}]/I[K\alpha_{1,2}M^{(0)}]$ yield ratio for which a value of 8.9% was chosen. This value was deduced from the analysis of the $K\beta_2M^{(1)}$ spectrum (see next section). K-L_3N RAE (radiative Auger effect [38]) transitions were found to contribute significantly to the intensity observed in the energy domain comprised between the $K\alpha_1$ and $K\alpha_2$ lines. The complex RAE structure was approximated by several juxtaposed Voigt profiles. The $K\alpha_{1,2}L^{(1)}$ and $K\alpha_{1,2}M^{(2)}$ satellites whose relative intensities are small ($<0.5\%$) were, however, not considered in that first part of the analysis. The fitted $K\alpha_{1,2}$ spectrum is shown in Fig. 3(a).

The $K\alpha_1L^{(1)}$ region, which was measured separately with a 28 times longer acquisition time, was then analyzed. The intensity observed in this energy region is due mainly to the high-energy tails of the $K\alpha_{1,2}$ and $K\alpha_{1,2}M^{(1)}$ lines. The single evidence for the weak $K\alpha_1L^{(1)}$ satellite resides in a small excess of intensity appearing in the center of the domain. For this reason, we determined first the shape of the curve corresponding to the sum of the tails, keeping fixed the fit parameters at the values obtained previously from the analysis of the $K\alpha_{1,2}$ spectrum. The intensity of the $K\alpha_1$ line, however, was let free and used as an adjustable scaling factor. Furthermore, the interval corresponding to the expected position of the satellite (18 points) was not included in the fit. The obtained tail was then subtracted from the measured spectrum and the resulting residual L-satellite yield fitted, using three Voigt profiles to reproduce the satellite shape. The energies, widths, and intensities of the three Voigtians were let free in the fit. The $K\alpha_1L^{(1)}$ spectrum with the fitted components is shown in Fig. 3(b). The relative satellite intensity obtained from the fit is

$$\frac{X_{K\alpha_1L^{(1)}}}{X_{K\alpha_1L^{(0)}}}=(0.23\pm0.04)\%.$$

C. Krypton $K\beta_2$ spectrum

The krypton $K\beta_2$ spectrum was analyzed with four components, one for the diagram line, two for the first-order satellite, and one for the second-order satellite. All components were given a Voigt profile with a fixed 4.0-eV Lorentzian width and a free Gaussian width. The fitted spectrum is shown in Fig. 5. The Gaussian widths obtained from the fit vary between 4.8 eV for the diagram line and 7.1 eV for the second-order satellite whereas widths of 6.3 and 6.6 eV are found for the two components pertaining to the first-order satellite. In general, the Lorentzian width of a complex transition such as $K\beta_2M^{(n)}$ can be approximated by

$$\Gamma(K\beta_2M^{(n)})\cong\Gamma_K+\Gamma_{N_{2,3}}+n\Gamma_M, \qquad (3)$$

where Γ_X is the total width of the level X and n the number of spectator holes in the M shell. As a consequence, the Voigt profiles broaden with the satellite order. In our case, since the $K\beta_2$ spectrum was fitted with the same Lorentzian width for all components, the broadening of the four Voigtians is reflected by the above-mentioned increase of the Gaussian widths in function of the satellite order. Regarding the intensities, the following relative yields are obtained from the fit for the first- and second-order M satellites:

$$\frac{X_{K\beta_2 M^{(1)}}}{X_{K\beta_2 M^{(0)}}}=(8.91\pm 0.76)\% \quad \text{and} \quad \frac{X_{K\beta_2 M^{(2)}}}{X_{K\beta_2 M^{(0)}}}=(1.02\pm 0.13)\%.$$

D. Argon $K\alpha$ spectrum

The $K\alpha_1$ and $K\alpha_2$ diagram lines were fitted with two Lorentzians each, one for the main line, the second one for the unresolved M satellite (Fig. 7). All parameters were let free in the fit except the Lorentzian widths of the two main lines which were kept fixed at 1.5 eV and the yield ratios $I[K\alpha_2]/I[K\alpha_1]$ and $I[K\alpha_{1,2}M^{(1)}]/I[K\alpha_{1,2}M^{(0)}]$ which were set, respectively, at 0.507 (MCDF prediction) and 0.229 (from the analysis of the $K\beta$ spectrum, see Sec. III E). The L-satellite structure could be fitted satisfactorily with three Lorentzians (see inset of Fig. 7). From the fit an average energy shift of 19.4 ± 0.2 eV is obtained for the L satellite with respect to the parent diagram line whereas the relative satellite intensity is found to be

$$\frac{X_{K\alpha_{1,2}L^{(1)}}}{X_{K\alpha_{1,2}L^{(0)}}}=(2.46\pm 0.04\%).$$

E. Argon $K\beta$ spectrum

The $K\beta_{1,3}M^{(0)}$ diagram line and the $K\beta_{1,3}M^{(1)}$ and $K\beta_{1,3}M^{(2)}$ satellites could be fitted with a single Lorentzian each. All parameters were let free in the fitting procedure. The result of the analysis is shown in Fig. 8. The linewidths given by the fit for the main line and the two satellites are 1.6, 1.8, and 1.9 eV, respectively. The somewhat larger widths obtained for the $K\beta_{1,3}M^{(1,2)}$ transitions result from the numerous overlapping components contributing to the satellite structure. The obtained energy differences between the diagram line and the two satellites are 3.57 ± 0.01 and 8.04 ± 0.02 eV, respectively. Both values are nearly consistent with the results (3.7 ± 0.1 and 7.9 ± 0.1 eV) obtained by Deslattes *et al.* [1]. From the fit, the following relative intensities are found for the satellites:

$$\frac{X_{K\beta_{1,3}M^{(1)}}}{X_{K\beta_{1,3}M^{(0)}}}=(22.9\pm 0.1)\% \quad \text{and} \quad \frac{X_{K\beta_{1,3}M^{(2)}}}{X_{K\beta_{1,3}M^{(0)}}}=(3.9\pm 0.1)\%.$$

MCDF calculations show that the low-energy tail of the $3p^{(2)}$ satellite distribution extends down to the $K\beta_{1,3}M^{(1)}$ region and that the $3s^{(1)}$ satellite group is slightly overlapping with the $K\beta_{1,3}M^{(2)}$ transition. This partial overlap of the two satellites could not be taken into account in our analysis. It is thus possible that the above intensities of the two satellites are slightly overestimated by the fit.

IV. THEORY

The probability for either exciting or ionizing an electron from a bound orbital as a result of an inner-shell vacancy production can be calculated using the so-called sudden approximation [3,39–41]. In this model the atomic excitation is treated separately from the initial vacancy production process to which no reference is required except that the resulting change in the atomic potential due to the alteration in electron screening must be fast enough, specifically [7],

$$(E_{n'l'}-E_{nl})\Delta t/\hbar \ll 1, \tag{4}$$

where E_{nl} and $E_{n'l'}$ are the energies of the initial and final states, respectively, and Δt the time interval of the change in the Hamiltonian. For shake processes resulting from $1s$ photoionization, Sachenko and Demekhin [42] have shown that the condition (4) can be written as

$$\xi_{KS}:=\frac{I_s r_s}{\hbar v_K}\ll 1, \tag{5}$$

where I_S and r_S are, respectively, the ionization energy and mean radius of the subshell S undergoing the shake process and v_K the velocity of the K-shell photoelectron. An experimental study of the criterion (5) by Carlson and Krause [7] indicates, however, that this condition is unnecessarily severe and that for Ne the sudden approximation breaks down only above $\xi_{KL}\approx 0.2$. Studying the double ionization induced in Ne and Ti targets bombarded by electron and photon beams, Krause [43] found that the breakdown point of the sudden approximation appears to occur at

$$\varepsilon_{KS}:=(E_{e,ph}-E_K-E_S)/E_s\approx 10, \tag{6}$$

where the numerator represents the excess energy of the incident particle ($E_{e,\mathrm{ph}}$) over the ionization energy of the K-shell electron (E_K) plus the ionization energy of the shaken electron (E_S) which refers to an ion with a hole in an inner shell.

The probability for an electron to be promoted by the sudden change of the atomic potential from the orbital nl to the orbital $n'l'$ (shakeup) or $\varepsilon' l'$ (shakeoff) is given by

$$P_{nl\to n'l',\varepsilon'l'}=\left|\int \psi_{nl}(Z)\psi^{*}_{n'l',\varepsilon'l'}(Z+\Delta Z)d\tau\right|^2, \tag{7}$$

where $\psi_{nl}(Z)$ and $\psi_{n'l',\varepsilon'l'}(Z+\Delta Z)$ are the initial and final state wave functions of the electron undergoing the transition and ΔZ represents the change of the effective charge resulting from the inner-shell core vacancy production. Note that according to selection rules (shake transitions are monopole transitions) l' must always be equal to l. For $\psi_{nl}(Z)$ single-electron wave functions from Hartree-Fock solutions of the neutral atom are usually used. For $\psi_{n'l,\varepsilon'l}(Z+\Delta Z)$ Hartree-Fock solutions of the ion with a single-hole configuration (single configuration shake calculations) or two-hole configurations (multiconfiguration shake calculations) can be employed.

If $n=n'$, Eq. (7) gives the probability for the electron to remain in its original orbital so that the probability for this electron to undergo a shake transition $n\to n',\varepsilon'$ can be written as

$$P_1=1-P_{nl\to nl}-P_F, \tag{8}$$

where P_F is a correction which accounts for forbidden shakeup transitions to already filled orbitals. The probability for exciting or ionizing one or more electrons from a subshell nl containing N electrons is thus [41]

$$P_N=1-\left[\left|\int \psi_{nl}(Z)\psi^{*}_{nl}(Z+\Delta Z)d\tau\right|^2\right]^N-P_F. \tag{9}$$

TABLE II. Relative x-ray satellite intensities $x_{S^{(h)}}$, relative primary vacancy yields $i_{S^{(h)}}$, and total shake probabilities P_S in percent [$x_{S^{(h)}}$ stands for $X_{K_qS^{(h)}}:X_{K_qS^{(0)}}$ and $i_{S^{(h)}}$ for $I(K^{(1)}S^{(h)}):I(K^{(1)}S^{(0)})$].

Target	$x_{L^{(1)}}$[a]	$i_{L^{(1)}}$	P_L	$x_{M^{(1)}}$[a]	$i_{M^{(1)}}$	P_M[b]	$x_{M^{(2)}}$[a]	$i_{M^{(2)}}$	P_M[c]
Ar	2.54(4)	2.73(20)	2.66(18)	22.9(1)	28.7(1.9)	21.6(1.0)	3.90(10)	3.40(35)	21.2(8)
Kr	0.26(4)	0.33(6)	0.33(5)	9.05(77)	8.47(95)	7.78(80)	1.04(13)	0.36(13)	8.0(1.3)

[a]Corrected for the differences in the x-ray tube intensity (see Table I).
[b]From first-order satellite.
[c]From second-order satellite.

Many performed shake calculations (e.g., [41,44]) are based on the above relation. Depending on the choice of the single-electron wave functions the results vary somewhat (see, e.g., Tables III and IV). This approach does not allow us, however, to get separate probabilities for shakeup and shakeoff transitions. To distinguish shakeup from shakeoff, the transition probabilities have to be calculated from the more complicated overlap integrals

$$P'_N=\left|\int \psi_{nl}(Z)\,\psi^*_{n'l',\varepsilon'l'}(Z+\Delta Z)\,d\tau\right|^{2N}, \qquad (10)$$

employing single-hole or multihole configuration for the final ionic state [45]. Separate shakeup and shakeoff probabilities can also be gained from MCDF calculations performed in the so-called dipole approximation [46,47].

V. RESULTS AND DISCUSSION

As mentioned in the Introduction, the shake probabilities were deduced from the yields of the L and M satellites relative to the parent diagram lines. It has to be noted, however, that the measured satellite yields reflect the distribution of the spectator holes at the moment of the K x-ray emission and not the initial distribution following the $1s$ photoionization which has to be known for the determination of the shake probabilities. Processes such as radiative, Auger, Coster-Kronig, and super Coster-Kronig transitions occurring prior to the K x-ray emission can indeed modify the number of the spectator holes created by the shake process. In order to extract the primary vacancy distributions from the observed satellite intensities, statistical scaling procedures which account for all those rearrangement processes preceding the K x-ray emission were applied. Details about such L- and M-shell rearrangement calculations are given for both elements in the Appendix. The relative satellite yields, corrected for the differences in the intensity I_{tube} of the x-ray tube radiation contributing to the $K^{(1)}$, $K^{(1)}L^{(1)}$, or $K^{(1)}M^{(1,2)}$ excitation of the targets (see Table I), and the deduced relative primary vacancy yields are presented for both elements in Table II. It can be seen that the rearrangement processes may increase or decrease the relative intensities of the satellites. In particular, one can notice that the intensity of the second-order M satellite of Kr is drastically enhanced by the atomic rearrangement.

If we assume that there is no correlation between the electrons ejected from the same shell by a shake process, the primary vacancy yields $I(K^{(1)}S^{(h)})$ ($S=L$ or M, $h=0$, 1, or 2) can be written as follows:

$$I(K^{(1)}S^{(h)})\sim\sigma_K^{\text{photo}}\binom{s}{h}p_S^h(1-p_S)^{s-h}, \qquad (11)$$

where σ_K^{photo} is the K-shell photoionization cross section, s the number of electrons in the shell S, p_S the average S-shell shake probability per electron, and $\binom{s}{h}$ the binomial coefficient. Using the simplified notations

$$i_{S^{(h)}}:=\frac{I(K^{(1)}S^{(h)})}{I(K^{(1)}S^{(0)})} \qquad (12)$$

the following equations for p_S are then obtained from Eq. (11):

$$\binom{s}{h}p_s^h=i_{S^{(h)}}(1-p_s)^h. \qquad (13)$$

Using the solutions of Eq. (13) for p_S, the total shakeoff plus shakeup probability P_S for a single ionization of the shell S is then given by

$$P_s=s\cdot p_s(1-p_s)^{s-1}. \qquad (14)$$

The experimental shake probabilities P_L and P_M of Ar and Kr deduced from Eq. (14) are presented in Table II. It is interesting to note that for both elements the values P_M extracted from the relative intensities of the first- and second-order satellites are consistent within the experimental uncertainties. It seems therefore that the two M electrons are ejected in a quasiuncorrelated way by the shake process, as assumed before.

Our experimental shake probabilities correspond to single excitations only, or double excitations only, and as such are not directly comparable with theoretical results deduced from Eq. (9) like those of Åberg [3], Carlson and Nestor [41], or Mukoyama and Tamiguchi [44], who have calculated probabilities of one or more electrons being excited from a given shell. Another difficulty is encountered when comparing our results with other experimental values because in some of the latter the shake probability is simply defined as the ratio of the satellite to diagram line intensity. For this reason, the theoretical and experimental results quoted in Tables III and IV were, if necessary, renormalized to correspond to the probability (14) of removing a single electron from a given subshell. The theoretical values labeled ''this work'' in Tables III and IV were computed in the framework of the sudden approximation model using the self-consistent Dirac-Fock wave functions from the code of Dyall [48].

In the relations (11) and (14) we have assumed tacitly that the S-shell shake probability per electron p_S is the same for

TABLE III. Theoretical and experimental shake probabilities of krypton in percent. All data were normalized to correspond to the probability defined by the relation (14).

Excited state	Experiment		Theory		
Kr	This work	[8][a]	[41]	[44]	This work
$1s^{-1}2s^{-1}$			0.06	0.06	0.05
$1s^{-1}2p^{-1}$			0.27	0.26	0.27
Total L-shell shake	0.33±0.06		0.33	0.32	0.32
$1s^{-1}3s^{-1}$			0.22	0.21	0.23
$1s^{-1}3p^{-1}$		1.3[b]	1.12	1.09	1.22
$1s^{-1}3d^{-1}$		5.1[c]	3.45	3.39	3.60
Total M-shell shake	7.84±0.68[d]	6.4[e]	4.79	4.69	5.05

[a]Relative photoexcitation cross sections (calculated in the dipole approximation for an incident photon energy of 17 025 eV).
[b]$1s^{-1}3p^{-1}4p-np\varepsilon p$ total shakeup probability of 0.1% included.
[c]$1s^{-1}3d^{-1}4d-nd\varepsilon p$ total shakeup probability of 1.3% included.
[d]Weighted average from first- and second-order satellites.
[e]$3s$-subshell shake probability not included.

all subshells, which is of course not completely correct. This approximation, however, modifies only slightly the total shake probability P_S given by Eq. (14), as shown in the following example. From Dyall's calculations [45] the probabilities of single and double excitation of M electrons following $1s$ ionization in Ar are 22.5% and 2.18%, respectively. The ratio of the single to double excitation is thus 10.3. In our simplified picture this ratio is given by

$$\frac{\binom{8}{1}p_M(1-p_M)^7}{\binom{8}{2}p_M^2(1-p_M)^6}=\frac{2(1-p_M)}{7p_M}. \tag{15}$$

Setting in Eq. (15) $p_M=2.81\times10^{-2}$ (Dyall's prediction for single excitation divided by the number of M electrons in Ar) results in a ratio of 9.9, in good agreement indeed with the above value of 10.3.

A. Krypton results

Krypton results are given in Table III. For the L shell a total shakeoff plus shakeup probability of 0.33%±0.06% is found from our measurements, in good agreement with various theoretical predictions based on the sudden approximation model. This is quite surprising because the Kr $K^{(1)}L^{(1)}$ excitation was induced by a photon beam with an average energy of 26.3 keV which lies below the breakdown point of the sudden approximation. Table I shows indeed that the parameter ξ_{KL} which should be smaller than 0.2 is equal to 0.65 whereas ε_{KL} which should be larger than about 10 is only 5.6. However, as there is no other experimental value available and because the experimental uncertainty of our result is quite large (about 20%), no definitive conclusion concerning the applicability of the sudden approximation (SA) model and the relevance of its predictions can be drawn in this case.

For the M shell the sudden approximation criteria (5) and (6) are well satisfied, yet SA predictions from different authors, ours included, seem to underestimate significantly the value of 7.84%±0.64% obtained in our experiment. Other calculations based on the dipole approximation give a result of 6.4% [8] which is closer to our experimental value but

TABLE IV. Same as Table III but for argon.

Excited state	Experiment				Theory				
Ar	[5][a]	[1][b]	[4][c]	This work	[3][d]	[41]	[44]	[45][e]	This work
$1s^{-1}2s^{-1}$					0.48	0.30	0.31	0.36/0.04	0.30
$1s^{-1}2p^{-1}$					2.55	1.59	1.58	2.13/0.27	1.75
Total L-shell shake	2.5±0.8			2.66±0.18	3.03	1.89	1.89	2.49/0.31	2.05
$1s^{-1}3s^{-1}$					3.1	2.4	2.5	2.9/1.8	2.8
$1s^{-1}3p^{-1}$					22.3	15.0	14.4	19.6/13.6	15.8
Total M-shell shake	20.7±1.4	23.6±1.2[f]	24.8±2.1[g]	21.4 ±0.6[h]	25.4	17.4	16.9	22.5/15.4[i]	18.6

[a]From photoelectron satellites.
[b]From $K\beta_{1,3}$ x-ray satellites.
[c]From $K-L_2L_3$ Auger satellites.
[d]Correction for shakeup transitions to already filled orbitals not included.
[e]The first number corresponds to the shakeoff plus shakeup probability, the second to the shakeup only.
[f]Weighted average from first- and second-order satellites (rearrangement correction included, see text).
[g]Shakeoff: 14.3%±1.5%, shakeup: 10.5%±1.5% (see text).
[h]Weighted average from first- and second-order satellites.
[i]Multiconfiguration shake calculations performed by the same author give 22.3% (total) and 14.7% (shakeup).

also smaller. These calculations were found to reproduce quite well the measured $1s3d$ double-photoexcitation cross sections (5.1%) but to underestimate somewhat the $1s3p$ cross sections (1.3% instead of 1.6%) [49]. Taking this difference into account and adding the 0.2% SA prediction for the $1s3s$ contribution (not included in the above 6.4%), one obtains a value of 6.9% which is almost consistent with our result. Furthermore, the total Kr shakeup plus shakeoff probability determined by the same group [8] by means of high-resolution photoelectron spectroscopy was found to be $36.8\% \pm 1.8\%$. Subtracting from this value the $1s4p$ and $1s4s$ contributions which are equal to 25.3% and 3.9%, respectively (dipole approximation predictions from [8]), and the 0.3% corresponding to the L-shell shake (this experiment) gives for the M shell a shake probability of 7.3% $\pm 1.8\%$, in good agreement with our experimental result.

B. Argon results

The Ar results are presented in Table IV. Regarding the L shell, the single other experimental value that we have found in the literature was obtained from photoelectron satellites [5]. A value of $2.5\% \pm 0.8\%$ is quoted, in fair agreement with our result of $2.66\% \pm 0.18\%$. The photoelectron spectrum was produced by bombarding the target with Ti $K\alpha$ x rays whose energy (4.5 keV) is smaller than the average bremsstrahlung energy used in our experiment (8.8 keV) (cf. Table I). This difference in the energy of the photons used for the target excitation explains perhaps the somewhat larger value obtained in our experiment. Theoretical predictions from the sudden approximation, except those of Dyall [45], seem to underestimate by about 30% the $K^{(1)}L^{(1)}$ excitation. The value computed by Åberg ($\sim 3\%$) [3] is larger than other theoretical predictions mainly because the forbidden transitions to already occupied orbitals were not excluded in his calculations.

Existing experimental information concerning Ar M-shell shake probabilities is presented in Table IV. At first, one can notice that an excellent agreement between our value ($21.4\% \pm 0.6\%$) and the result obtained by Krause, Carlson, and Dismukes [5] is observed. In the experiment of Deslattes and co-workers [1] relative yields of about 27% and 5% with respect to the diagram line were found for the $K\beta_{1,3}M^{(1)}$ and $K\beta_{1,3}M^{(2)}$ satellites (data corresponding to the 10-keV electron beam). Assuming relative uncertainties of 10% and 20%, respectively, for the intensities of the two satellites, the above values lead to shake probabilities of $20.5\% \pm 1.1\%$ and $24.3 \pm 1.7\%$ which are somewhat inconsistent. However, if the satellite yields are corrected to account for the rearrangement processes described in the Appendix, values of $23.5\% \pm 1.5\%$ and $23.8\% \pm 1.9\%$ are found, which are internally consistent but approximately 10% larger than our result. In the K-$L_{2,3}L_{2,3}$ Auger spectrum of an Ar gas jet target irradiated by hard photons from a synchrotron radiation source, Armen *et al.* [4] observed below the diagram line two bumps which were attributed to shakeup and shakeoff M-shell excitations as a result of the $1s$ photoionization. From the relative yields of the two low-energy satellites ($14\% \pm 2\%$ and $19\% \pm 2\%$, respectively, for the shakeup and shakeoff components) a total shakeup-shakeoff probability of $33\% \pm 4\%$ is obtained. This result, which is much larger than other experimental values, does not correspond, however, to the definition of the shake probability used in our study. We have thus recalculated by means of the method presented before the partial shake probabilities corresponding to the relative satellite yields quoted in [4]. From Eq. (11) the following system of equations is obtained for the shakeup p_{su} and shakeoff p_{so} probabilities per electron:

$$\frac{8p_{\mathrm{su}}}{(1-p_{\mathrm{su}})(1-p_{\mathrm{so}})^8} = 0.14, \tag{16a}$$

$$\frac{8p_{\mathrm{so}}}{(1-p_{\mathrm{so}})(1-p_{\mathrm{su}})^8} = 0.19. \tag{16b}$$

Introducing the solutions $p_{\mathrm{su}} = 1.46 \times 10^{-2}$ and $p_{\mathrm{so}} = 2.07 \times 10^{-2}$ of Eq. (16) in Eq. (14) leads to shake probabilities $P_{\mathrm{su}} = 10.5\% \pm 1.5\%$ and $P_{\mathrm{so}} = 14.3\% \pm 1.5\%$, i.e., $P_M = 24.8\% \pm 2.1\%$, a result which is almost consistent with our value.

The average energy of the ionizing radiation used for the Ar $K^{(1)}M^{(1)}$ excitation lies far above the break point of the sudden approximation (see Table I). A comparison of our experimental result with SA predictions is thus meaningful. As shown in Table IV, our value is more or less well reproduced by the SA model, depending on the choice of the single-electron wave functions. There is, however, a general trend of the sudden approximation calculations to underestimate the experimental values. It is also intriguing to note that Dyall's calculations (22.5%) which are in good agreement with the average value of the experimental results quoted in Table IV ($21.9\% \pm 0.6\%$) predict a ratio $P_{\mathrm{su}}:P_{\mathrm{so}}$ of 2.2 in strong disagreement with the ratio of 0.74 obtained from Eq. (16). A tentative explanation of this discrepancy can be found in Ref. [4].

ACKNOWLEDGMENTS

We wish to thank Dr. M. Polasik (University of Torun, PL) for the numerous MCDF calculations which have been very useful for the data analysis. This work was partly supported by the Swiss National Science Foundation.

APPENDIX: REARRANGEMENT PROCESSES

The probability W_p for a process, modifying the number of holes in the subshell X_i, to occur before the $K^{(1)}X_i^{(1)}$ doubly ionized state decays is given by

$$W_p = \frac{\Gamma_p}{\Gamma_K + \Gamma_{X_i}}, \tag{A1}$$

where Γ_p is the transition width of this particular process and Γ_K and Γ_{X_i} are the total widths of the K shell and the subshell X_i.

L-shell rearrangement

For $KL^{(n)}$ satellites the electron rearrangement is governed by LMX Auger transitions and L radiative transitions. The diagram and satellite x-ray emission yields $X_{K_qL^{(n)}}$ ($K_q = K\alpha_1$ for Kr and $K\alpha_{1,2}$ for Ar, n denotes the number of

TABLE V. Natural level widths in eV. All values are taken from Ref. [50] except where noted in the footnotes.

Target	Γ_K	Γ_{L_1}	Γ_{L_2}	Γ_{L_3}	Γ_{M_1}	Γ_{M_2}	Γ_{M_3}	$\Gamma_{M_{4,5}}$
Ar	0.68(3)	1.63(49)	0.126(32)	0.128(26)	0.38(8)[a]	$<10^{-4}$[b]	$<10^{-4}$[b]	
Kr	2.75(11)	4.3(1.3)	1.31(33)	1.17(23)	5.25[c]	1.80[d]	1.48[d]	<0.09[b]

[a]Extrapolation from super Coster-Kronig coefficients S_M [59].
[b]From [59].
[c]From [60] (theory).
[d]From [61] (experiment, no uncertainty quoted).

spectator holes in the L shell) are related to the initial vacancy yields $I_{KL^{(n)}}$ by the following equations:

$$X_{K_qL^{(0)}}=(I_{KL^{(0)}}+R_LI_{KL^1}+R_L^2I_{KL^{(2)}})\omega_{K_qL^{(0)}}, \quad \text{(A2)}$$

$$X_{K_qL^{(1)}}=(I_{KL^{(1)}}+R_LI_{KL^{(2)}}-R_LI_{KL^{(1)}})\omega_{K_qL^{(1)}}, \quad \text{(A3)}$$

where R_L is a scaling factor describing the electron rearrangement and $\omega_{K_qL^{(n)}}$ the partial K-shell fluorescence yield of the transition K_q with n spectator holes in the L shell. In accordance with the relation (A1) the subshell rearrangement coefficients R_{L_i} are given by

$$R_{L_i}=\frac{\Gamma_{L_i}}{\Gamma_K+\Gamma_{L_i}}. \quad \text{(A4)}$$

The factor R_L can be written as the weighted sum of the coefficients R_{L_i} minus the contribution of the Coster-Kronig transitions which do not change the number of L holes:

$$R_L=\sum_i w_{L_i}R_{L_i}-\sum_{i,j}\frac{w_{L_i}\Gamma_{L_iL_jX}}{\Gamma_K+\Gamma_{L_i}}=\sum_i w_{L_i}R_{L_i}\left(1-\sum_j f_{ij}\right), \quad \text{(A5)}$$

where X stands for M or N and f_{ij} represent the relative Coster-Kronig yields. Assuming that the number of initial holes is proportional to the calculated subshell shake probabilities, one finds the following weighting factors:

$$w_{L_i}=0.167, \quad w_{L_2}=0.285, \quad w_{L_3}=0.548 \quad \text{(Kr)},$$

$$w_{L_1}=0.144, \quad w_{L_2}=0.288, \quad w_{L_3}=0.568 \quad \text{(Ar)}.$$

Using the K and L_i level widths quoted by Krause and Oliver [50] with the indicated uncertainties (see Table V) and the Coster-Kronig coefficients f_{ij} calculated by McGuire [51] ($\sim$20% uncertainty), the following total rearrangement factors R_L are obtained:

$$R_L=0.256\pm0.026 \quad \text{(Kr)},$$

$$R_L=0.138\pm0.024 \quad \text{(Ar)}.$$

The production through shake processes of $K^{(1)}L^{(2)}$ excited states is expected to be very small. For Kr and Ar, values of $\sim5\times10^{-6}$ and $\sim2\times10^{-4}$, respectively, are indeed obtained from theoretical predictions based on the sudden approximation model. The yields $I_{KL^{(2)}}$ can thus be neglected in Eqs. (A2) and (A3) from which one obtains

$$\frac{I_{KL^{(1)}}}{I_{KL^{(0)}}}=\frac{(X_{K_qL^{(1)}}/X_{K_qL^{(0)}})(\omega_{K_qL^{(0)}}/\omega_{K_qL^{(1)}})}{1-R_L[1+(X_{K_qL^{(1)}}/X_{K_qL^{(0)}})(\omega_{K_qL^{(0)}}/\omega_{K_qL^{(1)}})]}. \quad \text{(A6)}$$

The partial fluorescence yields are given by

$$\omega_{K_qL^{(n)}}=\frac{\Gamma_{K_qL^{(n)}}}{\Gamma_{KL^{(n)}}}\omega_{KL^{(n)}}, \quad \text{(A7)}$$

where $\Gamma_{KL^{(n)}}$ is the total radiative width of the $K^{(1)}L^{(n)}$ state and $\Gamma_{K_qL^{(n)}}$ the width of the transition $K_qL^{(n)}$. These widths were deduced from MCDF calculations whereas the K-shell fluorescence yields $\omega_{KL^{(n)}}$ were approximated by (R stands for radiative and A for Auger)

$$\omega_{KL^{(n)}}=\frac{\Gamma^R_{KL^{(n)}}}{\Gamma^R_{KL^{(n)}}+\Gamma^A_{KL^{(n)}}}\cong\frac{\varepsilon^R_{KL^{(n)}}\Gamma^R_K}{\varepsilon^R_{KL^{(n)}}\Gamma^R_K+\varepsilon^A_{KL^{(n)}}\Gamma^A_K}$$

$$=\frac{\varepsilon^R_{KL^{(n)}}\omega_K}{\varepsilon^R_{KL^{(n)}}\omega_K+\varepsilon^A_{KL^{(n)}}(1-\omega_K)}. \quad \text{(A8)}$$

The coefficients $\varepsilon^{R,A}_{KL^{(n)}}$ are defined as follows:

$$\varepsilon^{R,A}_{KL^{(n)}}=\sum_i w_{L_i}(1-\delta^{R,A}_{KL_i^{(n)}}), \quad \text{(A9)}$$

where the factors $\delta^{R,A}_{KL_i^{(n)}}$ indicate the percentage diminution of K-shell radiative or Auger yields which result from the incomplete electron occupation of the subshell L_i. These factors were simply computed by normalizing the decay rates by the relative electron population of the subshells involved in the considered transitions. The radiative and radiationless transition strengths were taken from [52] and [53], respectively, and the fluorescence yields ω_K from [54], leading to the following results:

$$\omega_{K\alpha_1L^{(0)}}=0.565\times0.643=0.363,$$

$$\omega_{K\alpha_1L^{(1)}}=0.573\times0.669=0.383 \quad \text{(Kr)},$$

$$\omega_{K\alpha_1L^{(0)}}=0.907\times0.118=0.107,$$

$$\omega_{K\alpha_1L^{(1)}}=0.878\times0.132=0.116 \quad \text{(Ar)}.$$

Information concerning K fluorescence yields of multiply ionized atoms is scarce. For light elements, however, some results were published. The calculations of Chen, Crasemann, and Matthews [55] which were found to agree quite well with experimental data [57,58] predict for Ne a ratio $\omega_{KL^{(1)}}:\omega_{KL^{(0)}}=1.11$. From Tunnel and Bhalla's predictions [56] values of 1.20 and 1.12 are obtained for Ne and Si, respectively, indicating a smooth decrease of the ratio with Z. In this respect the ratios of 1.12 (Ar) and 1.04 (Kr) obtained by means of our simple statistical model look reasonable. The relative uncertainty of the coefficients $\omega_{K_qL^{(n)}}$ was estimated to be about 5%.

Introducing the corrected x-ray intensities and the above-mentioned results in Eq. (A6), the following values are finally obtained for the initial L-vacancy ratios:

$$\frac{I_{KL^{(1)}}}{I_{KL^{(0)}}}=(0.33\pm0.06)\% \quad \text{(Kr)},$$

$$\frac{I_{KL^{(1)}}}{I_{KL^{(0)}}}=(2.73\pm0.20)\% \quad \text{(Ar)}.$$

M-shell rearrangement

For the M shell the situation is more complicated because $K^{(1)}M^{(2)}$ states are no longer negligible and because $M_iM_jM_k$ super Coster-Kronig transitions are energetically possible. Furthermore, $K^{(1)}L^{(1)}$ levels may decay to $K^{(1)}M^{(1)}$ states through LMN Auger and LLM Coster-Kronig transitions and to $K^{(1)}M^{(2)}$ states via LMM Auger transitions. In this case the electron rearrangement is described by the following relations:

$$X_{K_qM^{(0)}}=(I_{KM^{(0)}}+R_MI_{KM^{(1)}}+R_M^2I_{KM^{(2)}})\omega_{K_qM^{(0)}}, \tag{A10}$$

$$X_{K_qM^{(1)}}=(I_{KM^1}+R_MI_{KM^{(2)}}+T_LI_{KL^{(1)}}-R_MI_{KM^{(1)}} -S_MI_{KM^{(1)}})\omega_{K_qM^{(1)}}, \tag{A11}$$

$$X_{K_qM^{(2)}}=(I_{KM^{(2)}}+S_MI_{KM^{(1)}}+U_LI_{KL^{(1)}}-R_MI_{KM^{(2)}})\omega_{K_qM^{(2)}}. \tag{A12}$$

As $I_{KM^{(0)}}$ is equal to $I_{KL^{(0)}}$, $I_{KL^{(1)}}$ can be written as

$$I_{KL^{(1)}}=\frac{I_{KL^{(1)}}}{I_{KL^{(0)}}}I_{KM^{(0)}}. \tag{A13}$$

The primary vacancy yields $I_{KM^{(n)}}$ can thus be obtained from the following system of equations:

$$\begin{pmatrix} 1 & R_M & R_M^2 \\ T_L\dfrac{I_{KL^{(1)}}}{I_{KL^{(0)}}} & 1-R_M-S_M & R_M \\ U_L\dfrac{I_{KL^{(1)}}}{I_{KL^{(0)}}} & S_M & 1-R_M \end{pmatrix} \begin{pmatrix} I_{KM^{(0)}} \\ I_{KM^{(1)}} \\ I_{KM^{(2)}} \end{pmatrix}$$

$$= \begin{pmatrix} \dfrac{X_{K_qM^{(0)}}}{\omega_{K_qM^{(0)}}} \\ \dfrac{X_{K_qM^{(1)}}}{\omega_{K_qM^{(1)}}} \\ \dfrac{X_{K_qM^{(2)}}}{\omega_{K_qM^{(2)}}} \end{pmatrix}. \tag{A14}$$

The rearrangement factors are defined as follows:

$$R_M=\sum_i w_{M_i}\frac{\Gamma_{M_i}-\sum_j \Gamma_{M_iM_jN}}{\Gamma_K+\Gamma_{M_i}}, \tag{A15}$$

$$S_M=\sum_i w_{M_i}\frac{\sum_{j,k} \Gamma_{M_iM_jM_k}}{\Gamma_K+\Gamma_{M_i}}, \tag{A16}$$

$$T_L=\sum_i w_{L_i}\frac{\sum_{j,k} (\Gamma_{L_iM_jN_k}+\Gamma_{L_iL_jM_k})}{\Gamma_K+\Gamma_{L_i}}, \tag{A17}$$

$$U_L=\sum_i w_{L_i}\frac{\sum_{j,k} \Gamma_{L_iM_jM_k}}{\Gamma_K+\Gamma_{L_i}}. \tag{A18}$$

The weighting factors w_{M_i} are proportional to the relative abundance of the holes in the M_i subshells, i.e., to the probabilities of producing $K^{(1)}M_i^{(1)}$ states via shake processes. Using theoretical predictions based on the SA model, one finds

$$w_{M_1}=0.045, \quad w_{M_2}=0.080, \quad w_{M_3}=0.158,$$

$$w_{M_4}=0.288, \quad w_{M_5}=0.429 \quad \text{(Kr)},$$

$$w_{M_1}=0.134, \quad w_{M2}=0.294, \quad w_{M3}=0.572 \quad \text{(Ar)}.$$

The partial fluorescence yields $\omega_{K_qL^{(n)}}$ were determined with the statistical scaling method described for the L shell. For $K_qM^{(2)}$ transitions, however, Eq. (A9) was modified in the following way:

$$\varepsilon_{KM^{(2)}}^{R,A}=\sum_{i,j} w_{M_iM_j}(1-\delta_{KM_i^{(1)}M_j^{(1)}}^{R,A}),$$

$$\text{where} \quad w_{M_iM_j}=\frac{w_{M_i}w_{M_j}}{\sum_{i,j} w_{M_i}w_{M_j}}. \tag{A19}$$

As for the L shell, the radiative and radiationless yields were taken from Refs. [52] and [53] and the transition relative yields were deduced from MCDF calculations, leading to the following results:

$$\omega_{K\beta_2 M^{(0)}} = 0.0130 \times 0.643 = 0.0084,$$

$$\omega_{K\beta_2 M^{(1)}} = 0.0156 \times 0.644 = 0.0100,$$

$$\omega_{K\beta_2 M^{(2)}} = 0.0180 \times 0.645 = 0.0116, \quad \text{(Kr)},$$

$$\omega_{K\beta_{1,3} M^{(0)}} = 0.0927 \times 0.118 = 0.0109,$$

$$\omega_{K\beta_{1,3} M^{(1)}} = 0.0806 \times 0.119 = 0.0096,$$

$$\omega_{K\beta_{1,3} M^{(2)}} = 0.0735 \times 0.120 = 0.0088 \quad \text{(Ar)}.$$

For krypton the M_1 level width was taken from [60], the M_2 and M_3 ones from [61], and the $M_{4,5}$ ones from [59] (see Table V). The Γ_{MMN} Coster-Kronig and Γ_{MMM} super Coster-Kronig transition rates were determined by considering the values quoted by McGuire [62] and normalizing then the latter in order to get the total M-subshell widths listed in Table V. Similarly, the Γ_{LMM} and Γ_{LMN} Auger transition rates were determined by normalizing the yields given in [53] with the L-subshell widths from [50]. The rearrangement factors were then computed, leading to the following results:

$$R_M = 0.064(7), \quad S_M = 0.040(6), \quad T_L = 0.101(17),$$

$$U_L = 0.235(34) \quad \text{(Kr)}.$$

Introducing these values in Eq. (A14), one obtains finally for the initial M vacancy yield ratios:

$$\frac{I_{KM^{(1)}}}{I_{KM^{(0)}}} = (8.47 \pm 0.95)\%, \quad \frac{I_{KM^{(2)}}}{I_{KM^{(0)}}} = (0.36 \pm 0.13)\% \quad \text{(Kr)}.$$

For argon the level widths Γ_{M_i} $(i \geqslant 2)$ can be neglected because they are extremely small ($< \sim 10^{-4}$ eV) [59]. As we did not find in the literature any information about the width of the level M_1, the latter was determined by a double logarithmic extrapolation of the super Coster-Kronig coefficients $S_{M_{1,2}}$ and $S_{M_{1,3}}$ quoted by McGuire for elements with $Z \geqslant 20$ [59]. A value of 0.38 eV was obtained for which an uncertainty of 20% was estimated. The LMM Auger and LLM Coster-Kronig transition rates were taken from [51] and [54], respectively (uncertainties of 20–30%). Since M_1 holes decay almost completely by M_1MM super Coster-Kronig transitions and because MMN Coster-Kronig and LMN Auger transitions do not exist in the case of Ar, one obtains from the relations (A15)–(A18) the following rearrangement factors:

$$R_M = 0.048(6), \quad S_M = 0.048(6), \quad T_L = 0.095(29),$$

$$U_L = 0.107(16) \quad \text{(Ar)}$$

and finally from Eq. (A14) the desired primary M-vacancy yield ratios:

$$\frac{I_{KM^{(1)}}}{I_{KM^{(0)}}} = (28.7 \pm 1.9)\%, \quad \frac{I_{KM^{(2)}}}{I_{KM^{(0)}}} = (3.40 \pm 0.35)\% \quad \text{(Ar)}.$$

[1] R. D. Deslattes, R. E. La Villa, P. L. Cowan, and A. Henins, Phys. Rev. A **27**, 923 (1983).
[2] J. Tulkki, Phys. Rev. Lett. **62**, 2817 (1989).
[3] T. Åberg, Phys. Rev. **156**, 35 (1967).
[4] G. B. Armen *et al.*, Phys. Rev. Lett. **54**, 182 (1985).
[5] M. O. Krause, T. A. Carlson, and R. D. Dismukes, Phys. Rev. **170**, 37 (1968).
[6] A. Kodre, S. J. Schaphorst, and B. Crasemann, in *X-Ray and Inner-Shell Processes*, edited by T. A. Carlson, M. O. Krause, and S. T. Manson, AIP Conf. Proc. No. **215** (AIP, New York, 1990), p. 582.
[7] T. A. Carlson and M. O. Krause, Phys. Rev. **140**, 1057 (1965).
[8] D. L. Wark *et al.*, Phys. Rev. Lett. **67**, 2291 (1991).
[9] J. H. McGuire, J. Phys. B **17**, L779 (1984).
[10] M. S. Freedmann, Annu. Rev. Nucl. Sci. **24**, 209 (1974).
[11] R. J. Walen and C. Briançon, in *Atomic Inner-Shell Processes*, edited by B. Crasemann (Academic, New York, 1975), Vol. 1, p. 233.
[12] T. M. Luke and J. D. Talman, Phys. Rev. A **41**, 1350 (1990).
[13] J. H. McGuire, N. C. Deb, and O. L. Weaver, Nucl. Instrum. Methods Phys. Res. B **40/41**, 340 (1989).
[14] J. Hoszowska, J.-Cl. Dousse, and Ch. Rhême, Phys. Rev. A **50**, 123 (1994).
[15] S. Svensson, N. Martensson, and U. Gelius, Phys. Rev. Lett. **58**, 2639 (1987).
[16] S. Svensson *et al.*, J. Electron Spectrosc. Relat. Phenom. **47**, 327 (1988).
[17] B. Perny *et al.*, Phys. Rev. A **36**, 2120 (1987).
[18] M. Carlen *et al.*, Z. Phys. D **23**, 71 (1992).
[19] M. Carlen *et al.*, Europhys. Lett. **13**, 231 (1990).
[20] E. Storm and H. I. Israel, Nucl. Data, Sect. A **7**, 565 (1970).
[21] B. Galley and J.-Cl. Dousse, Phys. Rev. A **50**, 3058 (1994).
[22] Ch. Herren and J.-Cl. Dousse, Phys. Rev. A **53**, 717 (1996).
[23] W. Beer, P. F. A. Goudsmit, and L. Knecht, Nucl. Instrum. Methods Phys. Res. A **219**, 322 (1984).
[24] W. Schwitz, Nucl. Instrum. Methods **154**, 95 (1978).
[25] J. A. Bearden and A. F. Burr, Rev. Mod. Phys. **39**, 125 (1967).
[26] K. D. Sevier, At. Data Nucl. Data Tables **24**, 323 (1979).
[27] R. D. Cowan, in *The Theory of Atomic Structure and Spectra*, edited by D. L. Sharp and L. M. Simmons, Jr., Los Alamos Series in Basic and Applied Sciences (University of California Press, Berkeley, 1981), p. 526.
[28] J. Hoszowska, J.-Cl. Dousse, J. Kern, and Ch. Rhême, Nucl. Instrum. Methods Phys. Res. A **376**, 129 (1996).
[29] R. D. Deslattes and E. G. Kessler, Jr., in *Atomic Inner-Shell Physics*, edited by B. Crasemann (Plenum, New York, 1985), p. 181.
[30] F. James and M. Roos, Comput. Phys. Commun. **10**, 343 (1975).
[31] M. W. Carlen *et al.*, Phys. Rev. A **46**, 3893 (1992).
[32] M. Polasik (private communication).
[33] M. Polasik, Phys. Rev. A **40**, 4361 (1989).
[34] I. P. Grant *et al.*, Comput. Phys. Commun. **21**, 207 (1980).

[35] R. D. Deslattes, P. L. Cowan, R. E. LaVilla, and K. G. Dyall, in *X-Ray and Atomic Inner-Shell Physics*, edited by B. Crasemann (AIP, New York, 1982), p. 100.
[36] I. P. Grant, Int. J. Quantum Chem. **25**, 23 (1984).
[37] S. I. Salem and P. L. Lee, At. Data Nucl. Data Tables **18**, 233 (1976).
[38] T. Åberg, in *Atomic Inner-Shell Processes*, edited by B. Crasemann (Academic, New York, 1975), p. 353.
[39] F. Bloch, Phys. Rev. **48**, 187 (1935).
[40] L. G. Parrat, Rev. Mod. Phys. **31**, 616 (1959).
[41] T. A. Carlson and C. W. Nestor, Jr., Phys. Rev. A **8**, 2887 (1973).
[42] V. P. Sachenko and V. F. Demekhin, Zh. Eksp. Teor Fiz. **49**, 765 (1965), [Sov. Phys. JETP **22**, 532 (1966)].
[43] M. O. Krause, J. Phys. (Paris) Colloq. Suppl. 10 **32**, C4-67 (1971).
[44] T. A. Mukoyama and K. Tamiguchi, Phys. Rev. A **36**, 693 (1987).
[45] K. G. Dyall, J. Phys. B **16**, 3137 (1983).
[46] J. Tulkki and T. Åberg, J. Phys. B **18**, L489 (1985).
[47] J. Tulkki *et al.*, Z. Phys. D **5**, 241 (1987).
[48] K. G. Dyall, I. P. Grant, C. T. Johnson, F. A. Parpia, and E. P. Plummer, Comput. Phys. Commun. **55**, 425 (1989).
[49] S. J. Schaphorst *et al.*, Phys. Rev. A **47**, 1953 (1993).
[50] M. O. Krause and J. H. Oliver, J. Phys. Chem. Ref. Data **8**, 329 (1979).
[51] E. J. McGuire, Phys. Rev. A **3**, 587 (1971).
[52] J. H. Scofield, Phys. Rev. **179**, 9 (1969).
[53] M. H. Chen, B. Crasemann, and H. Mark, At. Data Nucl. Data Tables **24**, 13 (1979).
[54] M. O. Krause, J. Phys. Chem. Ref. Data **8**, 307 (1979).
[55] M. H. Chen, B. Crasemann, and D. L. Matthews, Phys. Rev. Lett. **34**, 1309 (1975).
[56] T. W. Tunnel and C. P. Bhalla, Phys. Lett. **86A**, 13 (1981).
[57] D. L. Matthews, B. M. Johnson, G. W. Hoffmann, and C. F. Moore, Phys. Lett. **49A**, 195 (1974).
[58] N. Stolterfoht, D. Schneider, P. Richard, and R. L. Kauffman, Phys. Rev. Lett. **33**, 1418 (1974).
[59] E. J. McGuire, Phys. Rev. A **5**, 1043 (1972).
[60] L. I. Yin *et al.*, Phys. Rev. A **9**, 1070 (1974); **17**, 1556 (1978).
[61] S. Svensson *et al.*, Phys. Scr. **14**, 141 (1976).
[62] E. J. McGuire, Phys. Rev. A **5**, 1052 (1972).
[63] J. P. Desclaux, At. Data Nucl. Data Tables **12**, 312 (1973).